Plasmonics
DOI 10.1007/s11468-012-9420-y

Comparative Study of Plasmonic Properties of Cysteine-Functionalized Gold and Silver Nanoparticle Aggregates

Anikó Szalai · Áron Sipos · Edit Csapó · László Tóth · Mária Csete · Imre Dékány

Received: 11 June 2012 / Accepted: 6 August 2012

Abstract The absorptance spectra of gold and silver nanoparticle (NP) aqueous dispersions were measured by UV–visible spectroscopy and computed numerically by finite element method. Both NPs were functionalized by L-cysteine amino acid (Cys) in order to develop aggregate-based localized surface plasmon resonance biosensors. Absorptance spectra measured at an analogous pH value of ~4.9 were compared, where Au-Cys conjugates have moderately split spectra with two commensurate maxima, while Ag-Cys conjugates exhibit the most pronounced secondary peak according to the highest degree of aggregation. The purpose of our theoretical study was to determine the simplest linear chain-like and wavy aggregate geometries, which result in maxima matching the measured peaks. The aggregates were characterized by N number and d diameter of NPs, g gap between the NPs, and t thickness of the L-cysteine covering. By tuning the angle of incidence and E-field oscillation direction in p-polarized light with respect to the aggregates, the contribution of longitudinal and transversal modes was varied. The comparison of measurements and computations revealed that spectra measured on bioconjugate dispersions include effects of numerous aggregates with various geometries, illuminated from different directions and are influenced by inter-aggregate coupling. Inspecting the normalized E-field distribution surrounding the aggregates, it was shown that fundamentally different multipolar modes can be identified at primary and secondary absorptance maxima, due to coupled plasmonic resonances on NPs.

Keywords Nanoparticle aggregates · LSPR spectra · Coupled plasmonic resonances · Array effect

A. Szalai · Á. Sipos · M. Csete (✉)
Department of Optics and Quantum Electronics,
University of Szeged,
Dóm tér. 9.,
6720 Szeged, Hungary
e-mail: mcsete@physx.u-szeged.hu

E. Csapó · I. Dékány
Supramolecular and Nanostructured Materials Research Group of the Hungarian Academy of Sciences, University of Szeged,
Aradi vértanuk tere 1.,
6720 Szeged, Hungary

L. Tóth · I. Dékány
Department of Medical Chemistry, Faculty of Medicine,
University of Szeged,
Aradi vértanuk tere 1.,
6720 Szeged, Hungary

Introduction

The localized surface plasmon resonance (LSPR) phenomenon on metal nanoparticles (NPs) illuminated by polarized light with proper wavelength is capable of realizing EM-field concentration, which makes NPs promising candidates for many applications. The understanding of how LSPR results in characteristic spectra influenced by the shape, size, and dielectric constant of individual metal NPs and by the optical properties of the surrounding dielectric medium makes it possible to design NP-based systems with desired spectral properties [1–3].

The high-intensity localized plasmon field accompanying the LSPR phenomenon makes it possible to improve sensitivity in bio- and photodetection. There are tremendous efforts in recent nanoscience and nanoplasmonics to develop nanosensors, which are based on the sensitivity plasmon resonance phenomena to the dielectric environment of plasmonic nanostructures [4]. In nanoparticle-based LSPR sensors, various surface treatment methods were developed to ensure good capability to realize specific detection [5].

Published online: 23 August 2012

Gold and silver particles are the most common noble metal NPs applied in sensing. The advantage of gold is the appearance of plasmon resonance in the visible region and the high chemical stability [6]. Although the plasmon resonance of silver NPs is at the boundary of UV–vis spectral regions, higher detection sensitivity is achievable via silver-based plasmonic biosensors due to narrower resonance peaks. Several examples prove in the literature that clusters of silver NPs result in secondary peaks red-shifted to the visible region [1, 7]. The coupled plasmon resonance oscillations on clusters of metal NPs govern the entire absorption spectrum, which exhibits various peaks depending on both the dielectric and geometrical parameters [8]. Detailed spectral studies indicated that the splitting on spectra correlates with the ensembles' size, while the height of the absorption peaks is proportional to the aggregate quantity [9].

Previous works in the literature indicated that the *E*-field oscillation direction has a significant effect on the characteristic spectral properties of extended aggregates. The simplest elongated aggregate geometries, e.g., dimers and linear chains of spherical particles, were studied in detail mainly for two specific cases of *E*-field oscillation direction parallel to symmetry axes of the ensembles. It was concluded that a primary peak appears on the spectrum due to transversal modes excited by light with *E*-field oscillation perpendicular to the aggregates' long axis, while the longitudinal modes excited by light with *E*-field oscillation parallel to long axes result in red-shifted maximum [10].

These representative examples prove that the tuning of aggregates' spectra is possible by tailoring their geometry and suggest further tuning possibilities via proper illumination directions, but these approaches have not been investigated in detail previously. In addition to the possibility of spectral engineering, further considerable advantage in the application of aggregate-based LSPR is that the coupling between nanoparticles results in strongly enhanced near field, which makes possible sensing with significantly higher sensitivity, than on stand-alone particles. However the *E*-field distribution on extended aggregates with different shape and its dependence on illumination directions have not been studied systematically previously.

Based on previous literature, biofunctionalization of NPs by L-cysteine results in cluster formation. In the presence of L-cysteine, noble metal colloid spheres collect a monomolecular covering and assemble into aggregates through hydrogen bonds formed between amino acids located on neighboring silver sphere surfaces [11, 12]. Our previous experimental studies have shown that the stability of Ag-Cys bioconjugates and the resulted degree of aggregation is strongly dependent on the pH as well as on biomolecule concentration, as a result of the pH-dependent reactivity of the amino groups [13].

Even though the already discovered properties make aggregates as sensing elements promising, caused by the complexity of their spectral response, application of aggregate-based LSPR sensors requires uncovering of the relationship between the LSPR spectra and the aggregates' geometry, as well as the effect of illumination conditions. This demand motivated our present work, as our purpose was to determine the simplest aggregate geometries that may account for the observed spectra and to analyze the effect of their orientation and interaction on absorptance peaks and on near-field distribution.

Methods and Materials

Preparation and Experimental Spectral Study of Silver and Gold Nanoparticle Dispersions

Materials

Gold(III) chloride trihydrate (99.9 %, Aldrich), silver nitrate (99.9 %, Molar), sodium citrate dihydrate (99 %, Aldrich), and sodium borohydride (99 %, Fluka) were used without further purification for synthesis of spherical gold and silver nanoparticle-containing aqueous dispersions. In all cases, the dispersions were prepared in Milli-Q ultrapure water.

Preparation of Bare Au and Ag Nanoparticles

For synthesis of bare spherical, citrate-reduced gold nanoparticles, the well-known Turkevich method was applied; the steps of the synthesis were published previously [14]. The silver colloids were prepared according to the preparation procedure in [13]. Namely, the Ag^+ ions were reduced with sodium borohydride using sodium citrate stabilizing agent as well.

Biofunctionalization by L-Cysteine

The prepared gold and silver nanoparticles were functionalized by L-cysteine by adding an aqueous solution of the applied amino acid to the appropriate amount of nanoparticle-containing dispersions. In all cases, the monomolecular coverage of both Au and Ag NPs with L-cysteine was formed. Before spectral characterization of the biofunctionalized NPs, the samples were being stirred for 2–3 h at room temperature. In our previously published works, we confirmed that the stability of the prepared amino acid-functionalized nanoparticle dispersions is strongly pH dependent [15]. In the work presented here, the pH of the samples was adjusted to pH ~ 4.9 by using 0.1 M HNO_3, HCl, and NaOH aqueous solutions. At this pH, the aggregation of both Au and Ag nanoparticles occurred.

Experimental Methods

The average particle size and size distribution of the synthesized nanoparticles were determined by TEM and dynamic light scattering (DLS) methods. TEM images were recorded on a Philips CM-10 instrument at 100 kV accelerating voltage.

The size distribution of the particles was calculated by using UTHSCSA Image Tool 2.00 software. In the case of DLS measurements, a Zetasizer Nano ZS ZEN 4003 apparatus (Malvern Ins., UK) was used. The effect of pH on stability of biofunctionalized nanoparticles was studied by UV–vis spectroscopy as well. The spectra were recorded in the λ=300-800-nm range using a 1-cm quartz cuvette, by applying Ocean Optics USB2000 (Ocean Optics Ins., USA) diode array spectrophotometer.

Computation of Absorptance Spectra by Finite Element Method

Absorptance spectra of biofunctionalized gold and silver NP aggregates with different geometries were computed by the finite element method (FEM) applying the RF module of Comsol Multiphysics software package (COMSOL AB). The purpose of this comparative study was to determine the simplest aggregate geometries that may account for different absorptance spectra observed on Au-Cys and Ag-Cys bioconjugate dispersions at analogous pH~4.9.

According to different degrees of aggregation observed via TEM measurements, absorptance spectra of linear Au-Cys bioconjugate chains were determined, while absorptance of linear and wavy aggregates made of Ag-Cys bioconjugates was also computed (Figs. 1 and 2). The inspected aggregates are characterized by the following geometrical parameters: N number of NPs, d diameter of the colloid spheres, t thickness of the surrounding Cys shell, and g interparticle gap (Fig. 1).

In wavelength-dependent FEM computations, tabulated data sets of Au and Ag dielectric parameters from the literature were interpolated with a spline fit [16]. The wavelength-dependent refractive indices of L-cysteine and water were taken into account with Cauchy formulas based on [17, 18]. The absorptance spectra of Au-Cys dispersions in λ=400–800-nm and of Ag-Cys dispersions in λ=300–800-nm intervals were computed with 10-nm resolution, then 1-nm resolution was applied around the maxima. First, the spectra of single noble metal particles were computed, taking d_{Au}=13.6±1.17 nm and d_{Ag}=8.25±1.25 nm mean values of single Au and Ag NP diameters into account, according to TEM measurements (insets in Fig. 2). Then, the effect of covering by monomolecular Cys shell with t=0.45-nm thickness was determined [13]. These two geometrical parameters were not varied during FEM computations performed to determine aggregate spectra, while the g interparticle gap was swept between g=0.6 nm, corresponding to overlapping shells, and g=0.875 nm, modeling the more probable nonintersecting case. The computed absorptance curves of aggregates with different geometrical-size parameters were normalized to each other to ensure the same apparent concentration; then, the measured curve was normalized to the computed absorptance peak which resulted in the best fit for secondary maxima (Fig. 2). The modification of the gap has a strong impact on the strength of interparticle coupling inside aggregates and also on the interaction between aggregates. Namely, aggregates with lengths commensurate with the applied P unit cell size have potential to interact. In order to inspect different types of near- and far-field interactions, we applied periodic boundary conditions at the vertical sides of unit cells consisting of vertically (Fig. 1a, c) or horizontally (Fig. 1b, d) aligned aggregates.

The effect of grating–coupling phenomena on periodically arrayed aggregates was analyzed based on comparison of spectra originating from vertical and horizontal arrays (Figs. 3, 4, and 5). The light incidence angle onto the array plane was varied by changing the φ polar angle, in order to ensure analogous α illumination direction with respect to the NP ensembles in vertical and horizontal arrays, while the E-field oscillation direction was always in the plane of incidence of p-polarized light. The α illumination direction is defined as the angle between the k_{photon} light wave vector and the long axes of the aggregate, i.e., $\alpha=90°-\varphi$ for horizontally aligned, while $\alpha=\varphi$ for vertically aligned aggregates. Both E-field and $k_{photon,\,II}$ light wave vector projections are varied with respect to the long axes of the aggregates, when φ angle of incidence is tuned (insets in Fig. 1).

Result and Discussion

Comparison of Measured and Computed Spectra on Au-Cys and Ag-Cys Aggregates at an Analogous pH~4.9

In experimental spectral study, a single absorptance peak was registered on dispersions of bare Au NPs at 521 nm, while on Ag NPs, the single absorption maximum appeared at 391 nm (blue curves in Fig. 2a, b). Based on FEM computations, the absorption maximum is expected in close proximity of measured spectral peaks, namely at 523 nm on bare d=13.6 nm Au NPs and at 398 nm on d=8.25 nm diameter Ag NPs in aqueous environment. Both peaks are in accordance with the Fröhlich condition, as the $\varepsilon_{Ag/Au,\,real}/\varepsilon_{H_2O} \approx -2$ relationship is validated (dark cyan curves in Fig. 2a, b) [2].

FEM computation revealed that covering by the L-cysteine monolayer results in slightly forward-shifted peaks at 525 nm on Au-Cys and at 402 nm on Ag-Cys core shell

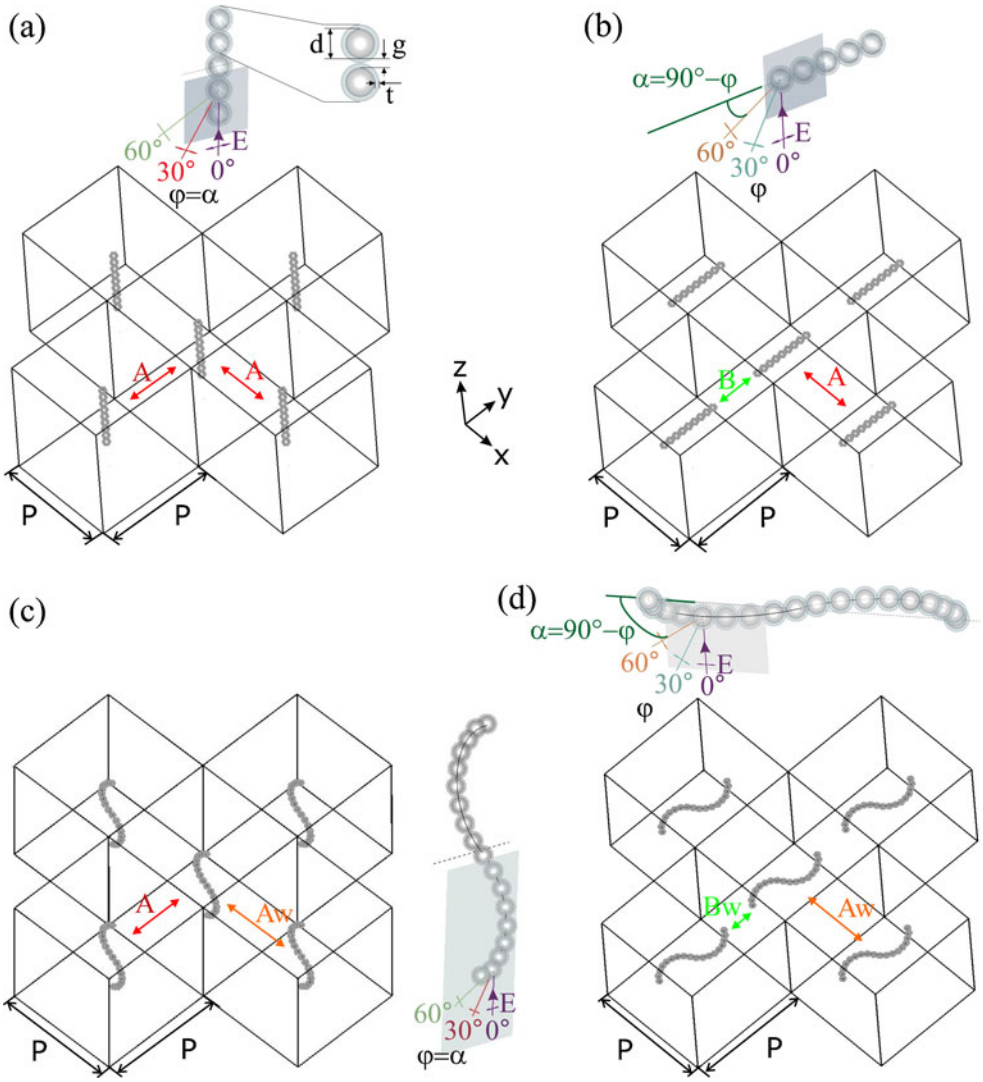

Fig. 1 **a**, **b** Schematic drawing of the investigated periodic aggregate arrays consisting of **a**, **c** vertically and **b**, **d** horizontally aligned **a**, **b** linear and **c**, **d** wavy aggregates inside unit cells with *P* size parameter. The drawings indicate A- and B-type couplings in horizontal arrays and only A-type coupling in vertical arrays. The Aw and Bw nominations refer to involvement of NP interactions located at different distances in neighboring wavy aggregates. The *insets* indicate the parameters used to characterize the linear and wavy aggregates and the method of φ polar angle tuning

NPs, indicating that silver NPs spectra are more sensitive to the modification in their dielectric environment (cyan curves in Fig. 2a, b). Spectra of both bare and L-cysteine-covered NPs are in spectral intervals of primary peaks measured on bioconjugates' dispersions revealing stand-alone particle contribution. However, the narrow peaks of stand-alone NPs cannot account for absorption observed in wide spectral regions on Au-Cys and Ag-Cys aggregates (wine curves in Fig. 2a, b).

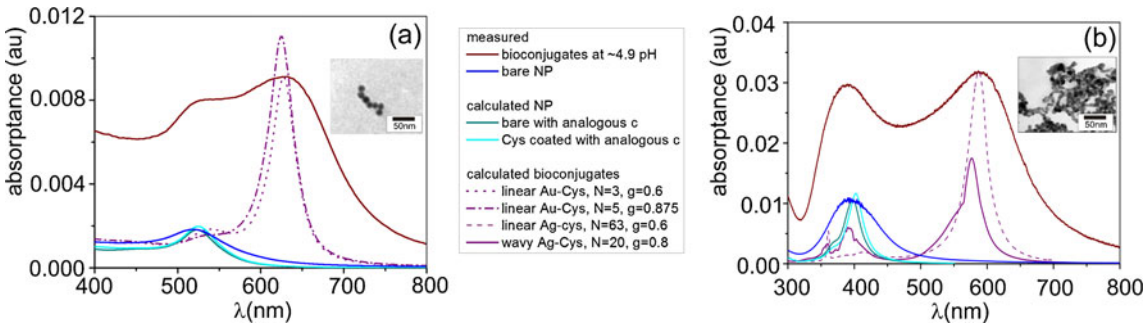

Fig. 2 The absorptance spectra of different **a** gold and **b** silver nanoparticle dispersions. The measured (*wine*) curves are registered at 4.95 pH value in Au-Cys and at 4.92 pH value in Ag-Cys dispersions. Absorptance curves measured on single NPs (*blue*) and computed by FEM for bare (*dark cyan*) and for cysteine-coated (*cyan*) single NPs with analogous concentration indicate peaks in the interval of primary maxima. Absorptance spectra of (a) two linear (*dot and dash-dot purple*), and (b) one linear (*dashed purple*), and one wavy (*solid purple*) aggregate exhibit maxima matching both the primary and secondary measured peaks. The *insets* indicate TEM pictures about the aggregates

Based on TEM investigations, the L-cysteine covering of noble metal NPs results in different types of aggregate formation, namely small and simple Au-Cys bioconjugate ensembles are observable in comparison to large and more complex Ag-Cys aggregates at an analogous pH of ~4.9 (insets in Fig. 2a, b).

In Fig. 2, the measured spectra are compared to spectra computed by applying horizontal aggregate arrays. The absorptance curve measured on Au-Cys bioconjugates indicates primary and secondary maxima corresponding to $\Delta\lambda$ ~96 nm split. The DSL measurements revealed a small average Au-Cys bioconjugate size of ~47 nm. Based on FEM computations, linear Au-Cys aggregates with similar length are capable of resulting in absorptance peaks in the interval of the measured primary and secondary absorptance maxima (Table 1). When overlapping shells are considered, aggregates consisting of three particles have maxima at 540 and 628 nm (dot purple curve in Fig. 2a). The more realistic nonintersecting shells result in good matching between the computed 625 nm and measured 631 nm secondary maxima (dash–dot purple curve in Fig. 2a). Although the entire length of the five-NP linear chain is larger than the average diameter measured by DLS, this Au-Cys aggregate geometry was selected to study the array and illumination direction effects, as intersection of covering biomolecule shells is less probable.

The absorptance curve on Ag-Cys bioconjugates indicates separated primary and secondary maxima corresponding to $\Delta\lambda$ ~197 nm split, which is approximately two times larger than the split observable on Au-Cys conjugates (Fig. 2b, Table 1). The higher sensitivity of the spectra to aggregation indicates that Ag-Cys bioconjugates ensure higher sensitivity in aggregate-based sensors. The DLS measurements indicated Ag-Cys aggregate average diameters approximately one order of magnitude larger than in the case of Au-Cys aggregates. FEM computations revealed that very long linear and medium-length wavy ensembles exhibit maxima at analogous spectral positions and with commensurate split, as the measured peaks. In the case of overlapping shells, 63 Ag NPs result in maxima at 414 and 587 nm ensuring an almost perfect match between the measured and computed secondary peaks (dashed purple curve in Fig. 2b). Wavy aggregates with nonintersecting shells result in maxima at 398 and 577 nm, i.e., providing good matching between the measured and computed primary peaks (solid purple curve in Fig. 2b). The computed split better approximates the measured $\Delta\lambda$ value in the case of the wavy Ag-Cys chain, and the absorption spectrum of the wavy Ag-Cys aggregate has larger FWHM similarly to the measured wide peaks. Both long linear and short wavy Ag-Cys aggregates were investigated to inspect the array- and illumination direction-related effects.

Comparison of Spectra Originating from Vertical and Horizontal Aggregate Arrays

In the case of vertically aligned aggregates, only A-type coupling is possible originating from the interaction of linear or wavy aggregates aligning parallel to each other at P distance, which equals with the length of the unit cell. This coupling is characteristic for aggregate arrays with P periodicity and involves all interactions between particles in neighboring parallel aggregates (Fig. 1a, c). A significant difference between the two investigated aggregate geometries is that in linear chains, the shortest distance between interacting particles in neighboring aggregates is the P periodicity in vertical arrays, while in wavy aggregates, also A-type coupling involves interaction of particles at distances either smaller or larger than P periodicity. The Aw-type coupling results in broadened spectral response according to the wider interval of distances between interacting particles.

The horizontal arrangement of the aggregates makes it possible for more types of coupling phenomena to be involved in collective plasmonic resonances. The B-type coupling is also at play, which involves all interactions between particles in neighboring aggregates at distances in $[P–L, P+L]$ interval in horizontal arrays of aggregates with L length aligning in cubical unit cells with P side. The strength of interaction is governed by the shortest distance between in-line aggregates, which equals with the $P–L$ distance between the ends of NP ensembles. Closely packed in-line ensembles have potential to enhance this B-type coupling due to near-field interaction (Fig. 1b, d).

The array effect may result in the appearance of additional absorptance peaks, when the adding of the light wave vector and the grating wave vector results in plasmon mode, the wavelength or multiple wavelength of which is commensurate with the aggregates' length. The grating-coupled plasmon wavelength can be calculated as:

$$\mathbf{k}_{\text{plasmon}} = \mathbf{k}_{\text{photon}} + n \cdot \mathbf{P}, \tag{1}$$

where $|\mathbf{P}| = 2 \cdot \pi / P$ reveals the grating wave vector corresponding to the P periodic unit cells. Resonant excitation occurs with nodes/antinodes at both ensemble ends, when the length of the aggregate is multiple of the half-plasmon wavelength:

$$L = m \frac{\lambda_{\text{plasmon}}}{2}, \tag{2}$$

while resonant oscillations with node–antinode pairs at ensemble ends occur when the length of the chain is odd-integer-times of quarter plasmon wavelength:

$$L = (2 \cdot m' - 1) \frac{\lambda'_{\text{plasmon}}}{4}. \tag{3}$$

Based on the analogy between NP ensembles and elongated antenna-like nano-objects, the phase pick-up upon reflection determines whether antinodes or nodes appear at the termination of the chain, i.e., whether a half or quarter wavelength of the resonant modes is commensurate with the chain [19].

An important difference between vertical and horizontal arrays is that in horizontal arrays, the $k_{\text{photon, II}}$ projection of the light wave vector along the NP ensemble is parallel to the **P** array wave vector along B-type coupling direction, while the $k_{\text{photon, II}}$ and **P** wave vectors are perpendicular to each other for all grating wave vectors in vertical arrays. As a result, the contribution of far-field coupling to resonant excitation of coupled plasmonic modes along NP arrays is predicted for horizontal arrays. The parallelism of the $k_{\text{photon, II}}$ photon wave vector projection to **P** grating vector along B-type coupling makes it possible to excite modes, which are unattainable in vertical arrays, i.e., more and larger absorptance peaks are expectable in horizontal arrays.

Effect of Au-Cys Aggregates' Orientation

In the case of perpendicular incidence (φ=0°) onto horizontal array of N=5 Au-Cys bioconjugate ensembles, a large absorptance peak is observable at 625 nm, while only a shoulder appears in the spectral interval of the measured primary peak, corresponding to ~7 ratio of absorptances (dash–dot purple curve in Fig. 2a and purple spectrum in Fig. 3). By increasing the angle of incidence to φ=30°, the red-shifted peak decreases, the shoulder becomes more pronounced, and appears at slightly smaller wavelength (blue spectrum in Fig. 3). At φ=60° incidence angle, a separated primary peak appears at ~520 nm, proving that small linear Au-Cys chains are capable of contributing to the absorptance in this spectral interval when they are illuminated at large polar angles. The secondary peak further decreases by increasing the angle of incidence (orange spectrum in Fig. 3).

Interestingly, the spectra of vertical arrays differ from the spectra of horizontal arrays at analogous α illumination directions (green-to-blue and red-to-orange spectra in Fig. 3). On the spectra of horizontal arrays, both primary and secondary extrema are noticeably forward shifted, and the red-shifted peaks are slightly smaller compared to the secondary maxima on spectra of vertical arrays.

Although there is a slight difference between the primary and secondary absorptance peaks on spectra of horizontal and vertical arrays, this small difference indicates that there is no symmetry breaking in the near field of the tiny Au-Cys aggregates caused by their nearest neighbors. The very small 72-nm length of the investigated Au-Cys linear chain does not promote near-field interaction in horizontal arrays, i.e., the observed differences may originate from different types of far-field couplings in horizontal and vertical arrays.

The near-field pictures indicate similar odd modes corresponding to m=1 at all secondary maxima, with E-field antinodes at the ends of the linear chains (pictures indicated by even numbers in Fig. 3). The intensity distribution is symmetrical in the case of perpendicular incidence, when the p-polarized light excites purely longitudinal modes (picture 2 in Fig. 3). The nodes are forward shifted along the propagation direction with increasing φ angle of incidence, when the transversal modes are gradually enhanced.

At the primary maxima, the tilting results in a significant change in the E-field distribution along the array (pictures indicated by odd numbers in Fig. 3). At perpendicular incidence, even modes appear corresponding to m=2 in contradiction with the literature predicting even modes only for oblique incidence or bent objects (picture 1 in Fig. 3) [20].

The α=60° illumination direction (φ=30°/60°) causes the appearance of one single node close to the exit/entrance side of the small chains in horizontal/vertical arrays. This reveals a different phase jump upon reflection in the spectral interval of the primary peak, which corresponds to a chain length commensurate with a quarter wavelength of the resonant modes (picture 3/5 in Fig. 3) [19]. When the angle between the beam and the chain is smaller, i.e., at α=30° (φ=60°/30°) in horizontal/vertical arrays, transversal modes become dominant, and the intensity modulation along the chain is less pronounced (picture 7/9 in Fig. 3). Even though the n=3 order grating coupling is capable of resulting in

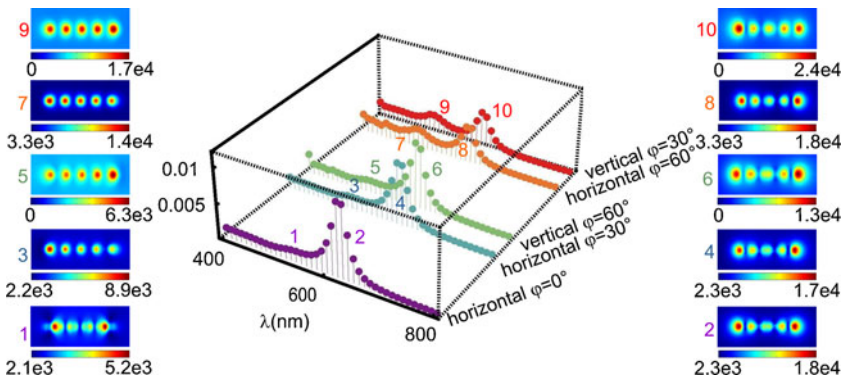

Fig. 3 Transformation of the split spectra of linear chain-like Au-Cys aggregates consisting of N=5 Au NPs arrayed at 0.8 nm gap, when the angle of incidence is 0° (*purple*), 30° (*blue*), and 60° (*orange*) in horizontal array, and 60° (*green*) and 30° (*red*) in vertical array. The *pictures* indicate the normalized E-field at the primary (*odd numbers*) and secondary (*even numbers*) peaks on the spectra

plasmonic mode excitation with half wavelengths equal to the chain length in all of the investigated cases, odd modes corresponding to $m'=1$ are dominant at the primary peak at oblique incidence (pictures indicated by odd numbers in Fig. 3, except picture 1).

Effect of Linear Ag-Cys Aggregates' Orientation

In the case of perpendicular incidence ($\varphi=0°$) onto horizontal array of linear chain-like aggregate consisting of $N=63$ Ag-Cys bioconjugates, the ratio of absorptances at the primary (414 nm) and secondary (587 nm) maxima is ~16 (dashed purple curve in Fig. 2b and purple spectrum in Fig. 4). When the light is incident at $\varphi=30°$ onto horizontal Ag-Cys array, the red-shifted peak decreases, while the UV peak increases, and appears at a smaller 400-nm wavelength (blue spectrum in Fig. 4). Further enhanced UV maximum appears at $\varphi=60°$ incidence angle at the same spectral position. These observations prove that long linear chains significantly contribute to the absorptance in the spectral interval of primary peak, when they are illuminated at large polar angles. The secondary peak is further decreased and is smaller than the primary peak at $\varphi=60°$ angle of incidence (orange spectrum in Fig. 4).

The spectra computed on long linear Ag-Cys chains more significantly depend on whether the elongated Ag-Cys aggregates are arrayed vertically or horizontally in the unit cells, than in the case of tiny Au-Cys ensembles (green-to-blue and red-to-orange spectra in Fig. 4). A slightly smaller primary peak appears in the vertical array illuminated at $\varphi=60°$ in comparison to the maximum observed, when the horizontally arrayed ensembles are illuminated at analogous $\alpha=60°$ direction. The secondary peak is more pronounced in the vertical Ag-Cys array similarly to the observation on Au-Cys bioconjugates (green-to-blue spectra in Fig. 4). In the case of $\varphi=30°$ angle of incidence onto vertical array of Ag-Cys chains, a split primary peak appears, with local maxima at smaller wavelengths, and a global maximum coincident with the primary maximum observed at analogous $\alpha=30°$ illumination direction of the horizontal chains. Interestingly, the absorptance is larger in vertical array at wavelengths before the global maxima, but larger maximal absorptance is reached in horizontal arrays. The red-shifted peak is smaller in vertical arrays than at analogous $\alpha=30°$ illumination direction of horizontal Ag-Cys chains (red-to-orange spectra in Fig. 4). The 558-nm length of the chain makes possible near-field interaction in horizontal arrays, as the 21-nm distance between the ensembles is commensurate with the decay length of the plasmon field at Ag–water bounding media.

At the secondary maximum, the $P=600$ nm periodic grating may result in coupling into modes corresponding to $m=3$ close to the investigated $\varphi=30°$ angle of incidence, while the condition of grating coupling to modes corresponding to $m=4$ is fulfilled at $\varphi=60°$ angle of incidence. The higher secondary peaks observed in the case of $\varphi=60°$ incidence angles are related to exactly met grating coupling condition.

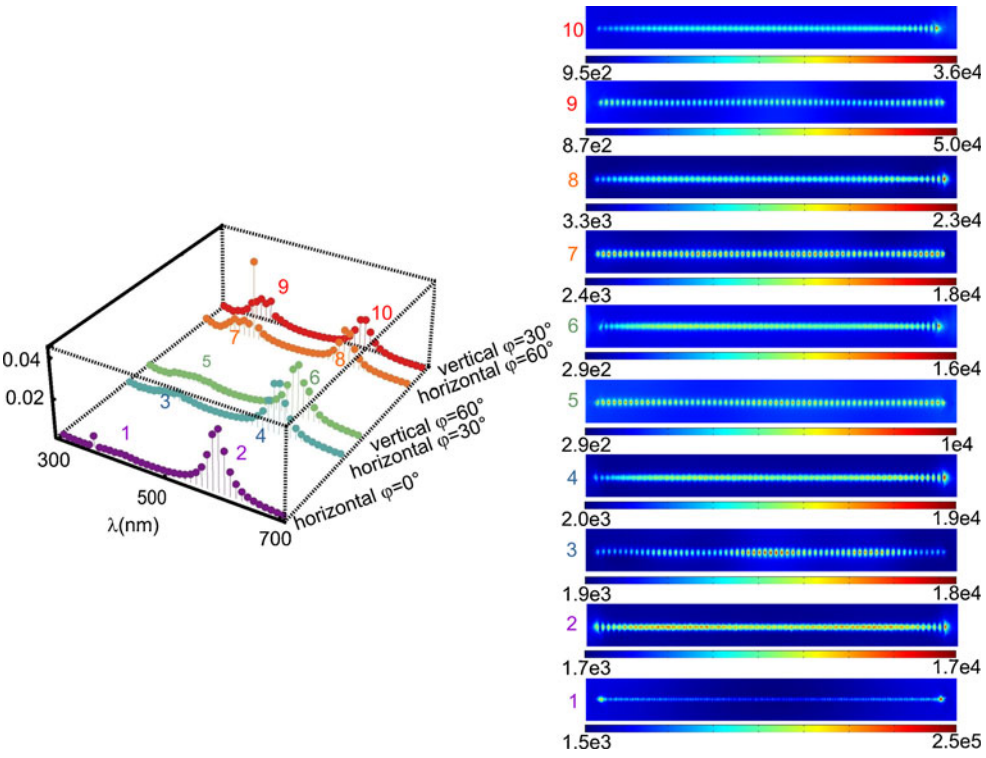

Fig. 4 Transformation of the split spectra of a linear Ag-Cys aggregate consisting of $N=63$ Ag NPs arrayed at 0.6 nm gap, when the angle of incidence is 0° (*purple*), 30° (*blue*), and 60° (*orange*) in horizontal array, and 60° (*green*) and 30° (*red*) in vertical array. The *pictures* indicate the normalized *E*-field at the primary (*odd numbers*) and secondary (*even numbers*) peaks on the spectra

The decreased primary peak in the case of vertical arrays in comparison to primary maximum on horizontal array illuminated at analogous α=60° reveals complex coupling effects. A larger primary peak, which is expected in the case of φ=60° angle of incidence due to the commensurability of the chain length with the half wavelength of grating-coupled modes corresponding to m=5, is not observable in vertical arrays. The observed tiny difference between the primary peaks on spectra of aggregates in horizontal and vertical arrays may originate partially from symmetry breaking in the near field of neighboring extended aggregates and might be related to the parallelism of the horizontal chains to the grating wave vector.

Theoretically, the grating coupling results in excitation of modes corresponding to m=4 at ~360 nm wavelength at φ=30° angle of incidence, while coupling to resonant modes corresponding to m=5 occurs around 400 nm at φ=60° angle of incidence. This incidence angle-dependent coupling efficiency explains the wavelength-dependent ratio between the primary peaks originating from vertical/horizontal arrays at analogous α=30° (φ=30°/60°) illumination directions.

The near-field images about the *E*-field distribution at the secondary peaks indicate interference of different coexistent modes on the long linear Ag-Cys chains. The intensity distribution reveals collective resonance oscillation corresponding to m=1 and m=2 in the case of perpendicular incidence, even though odd dipolar oscillation is expected based on excitation of longitudinal modes by p-polarized light (picture 2 in Fig. 4). At φ=30°/60° incidence angles, resonant modes predicted by grating coupling theory corresponding to m=3/4 are not observable on the aggregates in either of the horizontal or vertical arrays (pictures 4/8 and 10/6 in Fig. 5).

Similar complex collective oscillations are observable at the primary maxima (images indicated by odd numbers in Fig. 5). In horizontal array, the even/odd modes are noticeable at φ=30°/60° incidence angles in agreement with the theory predicting grating coupling to modes corresponding to m=4/5 at the primary peaks (picture 3/7 in Fig. 5). In vertical arrays, the effect of analogous grating coupling is less noticeable on the intensity distribution (picture 9/5 in Fig. 5). This proves that the parallelism of the long axes of the aggregates promotes efficient mode excitation via grating coupling in horizontal arrays. To inspect the contribution of different array effects that may be at play in vertical and horizontal arrays, a different aggregate geometry was also investigated.

Effect of Wavy Ag-Cys Aggregates' Orientation

The ratio of the primary (398 nm) and secondary (577 nm) maxima is ~3, when wavy aggregates of N=20 Ag-Cys bioconjugates are illuminated by perpendicularly incident light, i.e., the primary peak is the most pronounced in this geometry (solid purple curve in Fig. 2b and purple spectrum in Fig. 4). Illumination of the horizontal array consisting of wavy Ag-Cys ensembles at φ=30° causes a decreased red-shifted peak and a split UV peak (blue spectrum in Fig. 4). A further enhanced UV maximum appears at φ=60° incidence angle at the same spectral position without split. The secondary peak is smaller than the primary peak at φ=60° angle of incidence, i.e., the ratio of the absorptance values at the maxima is reversed at large φ polar angles (orange spectrum in Fig. 4).

The spectra modify in a different manner, when wavy Ag-Cys aggregates are illuminated in vertical instead of horizontal arrays, in comparison to the long linear Ag-Cys aggregates (green-to-blue and red-to-orange spectra in Fig. 5). The primary peak in the vertical array illuminated at φ=60° exhibits a similar split but is slightly smaller than the maximum on horizontal array at analogous α=60° illumination direction (green-to-blue spectra in Fig. 4). A single primary peak appears at φ=30° angle of incidence on the vertical array, but the absorptance is smaller than in NP

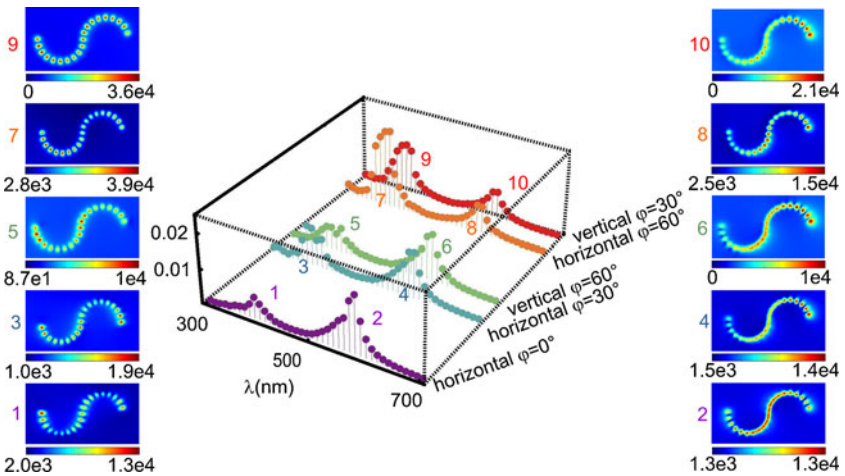

Fig. 5 Transformation of the split spectra of a wavy Ag-Cys aggregate consisting of N=20 Ag NPs arrayed at 0.8 nm gap, when the angle of incidence is 0° (*purple*), 30° (*blue*), and 60° (*orange*) in horizontal array, and 60° (*green*) and 30° (*red*) in vertical array. The *pictures* indicate the normalized *E*-field at the primary (*odd numbers*) and secondary (*even numbers*) peaks on the spectra

Table 1 Parameters (N, d, g) of each investigated aggregate geometry and (λ_1 and λ_2) positions of primary and secondary maxima on the measured/computed spectra, the corresponding $\Delta\lambda$ split, the L average aggregate diameter determined by DSL and the theoretical aggregate length applied in FEM computations

		N	d (nm)	g (nm)	λ_1 (nm)	λ_2 (nm)	L (nm)	$\Delta\lambda$ (nm)
Gold	Measured pH=4.95	–	13.6	–	535	631	47	96
	Linear I	3	13.6	0.6	540	628	43	88
	Linear II	5	13.6	0.875	Shoulder 542	625	72	83
Silver	Measured pH=4.92	–	8.25	–	391	588	523	197
	Linear	63	8.25	0.6	414	587	558	173
	Wavy	20	8.25	0.8	398	577	181/123	179

ensembles illuminated at α=30° in horizontal array (orange-to-red spectra in Fig. 4). The secondary red-shifted peaks are coincident in vertical and horizontal arrays of wavy Ag-Cys bioconjugates at analogous illumination directions.

The 123-nm length of the wavy Ag-Cys ensembles in 600-nm unit cells does not make possible near-field interaction in horizontal arrays caused by ten times larger distance between the wavy Ag-Cys aggregates in comparison to linear Ag-Cys chains. The same spectral position of the split on primary peaks observed in horizontal and vertical arrays at analogous α=60° illumination direction, as well as the strong polar angle dependence of maximal values, reveals different array effects. Namely, at φ=30° incidence angle, the n=2/1 order grating–coupling enables excitation of plasmon modes with wavelength, which is commensurate with the length of the wavy aggregate at the primary/secondary peak. When the light is incident at φ=60° angle onto the arrays, the n=3/1 order grating–coupling is capable of exciting plasmons with wavelength commensurate with the long axes of the wavy chain. The expected modes correspond to m=2/m=1 cases at the primary/secondary peaks.

The near-field pictures taken at the secondary maxima indicate E-field nodes in at least one end of the wavy aggregates. The intensity distribution reveals collective dipolar oscillation corresponding to m=1 in the case of perpendicular incidence, even though p-polarized light excites longitudinal and transversal modes simultaneously in wavy ensembles (picture 2 in Fig. 5).

At φ=30°/60° incidence angles, the entire wavy aggregate length seems to be commensurate with a quarter wavelength of the resonant modes corresponding to m'=1 (pictures 4/6 in Fig. 5) and m'=3 (pictures 10/8 in Fig. 5), rather than with a half wavelength. The expected decrease in wavelength, (namely by increasing the angle of incidence from 30° to 60° the half wavelength of modes should be commensurate with the long axes, instead of the chain length) is not noticeable (pictures 4 to 8 and 10 to 6 in Fig. 5). Interestingly, nodes are located at the entrance of the ensembles with respect to the propagation direction in both arrays at oblique incidence.

At the primary maxima, antinodes are observable at both the entrance and exit of the wavy ensemble (pictures indicated by odd numbers in Fig. 5). At perpendicular incidence and at α=60° illumination direction (φ=30°/60°), even modes appear corresponding to m=2 in agreement with the literature predicting even modes for bent objects (picture 1, 3, and 5 in Fig. 5) [20]. Interestingly, at α=30° illumination direction (φ=60°/30° in horizontal/vertical arrays), odd modes appear at the primary peak with antinodes at the wavy aggregates' ends (picture 7/9 in Fig. 5).

In horizontal array the equality of the wavy aggregate length with the wavelength of the dominant mode at φ=30° angle of incidence is in accordance with the prediction of n=2 order grating-coupled mode (picture 3 in Fig. 5). At φ=60° angle of incidence, a resonant mode corresponding to m=1 having a half wavelength equal with the long axis is observable in accordance with n=1 order grating-coupled mode, rather than the expected mode corresponding to n=3, m=2 cases (picture 7 in Fig. 5). However, the intensity distribution in vertical arrays is more similar at an analogous α illumination direction of the chains rather than at analogous φ incidence angles onto the arrays. This observation confirms that the relative orientation of the elongated NP ensembles with respect to the array plane plays a key role in determination of collective resonances.

Conclusion

The comparative study of Au-Cys and Ag-Cys bioconjugates' absorption was performed. FEM computations proved that fundamentally different and illumination direction-dependent collective plasmonic resonance oscillations appear at the primary and secondary peaks on spectra measured at the same pH ~4.9. Short linear chains of Au-Cys bioconjugates have spectra less sensitive to the aggregates' orientation and weakly effected by coupling on arrays with the investigated periodicity. Dipole-like collective oscillations appear along short Au-Cys chains at perpendicular incidence, which are transformed to transversal modes by

increasing the incidence angle more rapidly in horizontal arrays. Grating-coupled antenna-like mode development is observable also for oblique incidence at the secondary peak, while only for perpendicular incidence at the primary peak.

The spectra of very long linear chains of Ag-Cys aggregates are more sensitive to the illumination direction and exhibits both near- and far-field coupling-related array effects. The collective resonance oscillations originating from interference of coexistent modes involve antenna-like modes originating from grating–coupling on horizontal arrays of long linear chains.

Wavy Ag-Cys aggregates exhibit the largest primary peak, which becomes rapidly dominant by increasing the illumination angle. Antenna-like even and odd modes appear at the primary and secondary maxima, and modes originating from grating–coupling are identifiable at small incidence angles. Interestingly, the aggregates' orientation determines the near-field distribution, namely the same modes appear at analogous illumination directions with respect to the aggregates' long axes, rather than at the same angle of incidence onto the aggregate array.

The conclusion of the present study is that both spectral properties and near-field distribution might be controlled by appropriately illuminated horizontal arrays of extended aggregates with proper geometry. These findings are helpful in aggregate-based biosensor development and in the design of nanoparticle waveguides for wavelength-selective and directional signal transportation.

Acknowledgments The study was funded by the National Development Agency of Hungary with financial support from the Research and Technology Innovation Fund (CNK-78549) and OTKA K 75149. The publication is supported by the European Union and cofunded by the European Social Fund. Project title: "Broadening the knowledge base and supporting the long term professional sustainability of the Research University Centre of Excellence at the University of Szeged by ensuring the rising generation of excellent scientists." Project number: TÁMOP-4.2.2/B-10/1-2010-0012. This work is a part of the project "TÁMOP-4.2.1/B-09/1/KONV-2010-0005—Creating the Center of Excellence at the University of Szeged." The project named "TÁMOP-4.2.1/B-09/1/KONV-2010-0005—Creating the Center of Excellence at the University of Szeged" is supported by the European Union and cofinanced by the European Regional Development Fund.

References

1. Jensen T, Kelly L, Lazarides A, Schatz GC (1999) Electrodynamics of noble metal nanoparticles and nanoparticle clusters. J Clust Sci 10:295–317
2. Schuller A, Barnard ES, Cai W, Jun YC, White JS, Brongersma ML (2010) Plasmonics for extreme light concentration and manipulation. Nat Mater 9:193–204
3. Liz-Marzán LM (2006) Tailoring surface plasmons through the morphology and assembly of metal nanoparticles. Langmuir 22:32–41
4. Lal S, Link S, Halas NJ (2007) Nano-optics from sensing to waveguiding. Nat Photonics 1:641–648
5. Anker JN, Hall WP, Lyandres O, Shah NC, Zhao J, Van Duyne RP (2008) Biosensing with plasmonic nanosensors. Nat Mater 7:442–453
6. Daniel MC, Astruc D (2004) Gold nanoparticles: assembly, supramolecular chemistry, quantum-size-related properties, and applications toward biology, catalysis, and nanotechnology. Chem Rev 104:293–346
7. McFarland AD, Van Duyne RP (2003) Single silver nanoparticles as real-time optical sensors with zeptomole sensitivity. Nano Lett 3:1057–1062
8. Quinten M, Kreibig U (1993) Absorption and elastic scattering of light by particle aggregates. Appl Opt 32:6173–6182
9. Rosi NL, Mirkin CA (2005) Nanostructures in biodiagnostics. Chem Rev 105:1547–1562
10. Sweatlock LA, Maier SA, Atwater HA, Penninkhof JJ, Polman A (2005) Highly confined electromagnetic fields in arrays of strongly coupled Ag nanoparticles. Phys Rev B 71:235408
11. Mandal S, Gole A, Lala N, Gonnade R, Ganvir V, Sastry M (2001) Studies on the reversible aggregation of cysteine-capped colloidal silver particles interconnected via hydrogen bonds. Langmuir 17:6262–6268
12. Jing C, Fang Y (2007) Experimental (SERS) and theoretical (DFT) studies on the adsorption behaviors of L-cysteine on gold/silver nanoparticles. Chem Phys 332:27–32
13. Csapó E, Patakfalvi R, HornokV TL, Sipos Á, Szalai A, Csete M, Dékány I (2012) Plasmonic properties of biofunctionalized silver nanoparticles at different pH. Colloids Surf B 98:43–49
14. Majzik A, Fülöp L, Csapó E, Bogár F, Martinek T, Penke B, Bíró G, Dékány I (2010) Functionalization of gold nanoparticles with amino acid, β-amyloid peptides and fragment. Coll Surf B 81:235–241
15. Szalai A, Sipos Á, Csapó E, Hornok V, Tóth L, Csete M, Dékány I (2011) Numerical investigation of the plasmonic properties of bare and cysteine-functionalized silver nanoparticles. Plasmonics: Metallic Nanostructures and Their Optical Properties IX, edited by Mark I. Stockman, Proceedings of the SPIE, 8096:80963B
16. Palik ED (1998) Handbook of optical constants of solids. Academic, San Diego
17. Arwin H (1986) Optical properties of thin layers of bovine serum albumin, γ-globulin, and hemoglobin. Appl Spectrosc 40:313–318
18. Daimon M, Masamura A (2007) Measurement of the refractive index of distilled water from the near-infrared region to the ultraviolet region. Appl Opt 46:3812–3820
19. Barnard ES, White JS, Chandran A, Brongersma ML (2008) Spectral properties of plasmonic resonator antennas. Opt Express 16:16529–16537
20. Laurent G, Félidj N, Aubard J, Lévi G, Krenn JR, Hohenau A, Schider G, Leitner A, Aussenegg FR (2005) Evidence of multipolar excitations in surface enhanced Raman scattering. Phys Rev B 71:045430